Research Article Vol. 10, No. 9 / September 2023 / Optica 1153

OPTICA

Efficiency-boosted semiconductor optical amplifiers via mode-division multiplexing

Yi Wang,[1,*] Yihui Wei,[1] Victor Dolores-Calzadilla,[1,2] Daoxin Dai,[3,4] Kevin Williams,[1] Meint Smit,[1] and Yuqing Jiao[1]

[1]Eindhoven Hendrik Casimir Institute (EHCI), Eindhoven University of Technology, Eindhoven 5600MB, The Netherlands
[2]Photonic Integration Technology Center (PITC), Eindhoven University of Technology, Eindhoven 5600MB, The Netherlands
[3]State Key Laboratory for Modern Optical Instrumentation, Center for Optical & Electromagnetic Research, College of Optical Science and Engineering, International Research Center for Advanced Photonics, Zhejiang University, Zijingang Campus, Hangzhou 310058, China
[4]Jiaxing Key Laboratory of Photonic Sensing & Intelligent Imaging, Intelligent Optics & Photonics Research Center, Jiaxing Research Institute, Zhejiang University, Jiaxing 314000, China
*y.wang10@tue.nl

Received 17 March 2023; revised 26 July 2023; accepted 2 August 2023; published 24 August 2023

Semiconductor optical amplifiers (SOAs) are a fundamental building block for many photonic systems. However, their power inefficiency has been setting back operational cost reduction, circuit miniaturization, and the realization of more complex photonic functions such as large-scale switches and optical phased arrays. In this work, we demonstrate significant gain and efficiency enhancement using an extra degree of freedom of light—the mode space. This is done without changing the SOA's material design, and therefore high versatility and compatibility can be obtained. Light is multiplexed in different guided modes and reinjected into the same gain section twice without introducing resonance, doubling the interaction length in a broadband manner. Up to 87% higher gain and 300% higher wall-plug efficiency are obtained in a double-pass SOA compared to a conventional single-pass SOA, at the same operating current, in the wavelength range of 1560–1580 nm.

https://doi.org/10.1364/OPTICA.489894

1. INTRODUCTION

The pursuit of high energy efficiency has fueled major advances in photonic microchips, as it promises denser integration, lower costs, and reduced environmental impact of advanced technologies [1–5]. However, the semiconductor optical amplifier (SOA), a crucial element in photonic integrated circuits (PICs), still suffers from being very power-hungry and inefficient, particularly when weak signals are to be amplified. For an SOA before saturation, the same electrical power is needed to maintain a certain optical gain, regardless of the input optical power. This is due to the fact that the strength of stimulated emission depends linearly on the local photon density itself [6]. Consequently, the injected carriers are not efficiently utilized for stimulated emission before the photon density is sufficiently high, resulting in an overall low wall-plug efficiency (WPE) and uneven depletion of carriers. Furthermore, when signals are low, high levels of amplified spontaneous emission (ASE) are generated, contributing to increased noise rather than signal amplification.

Several approaches have been taken to improve the SOA's energy efficiency, including increased optical confinement [7–9], deeper quantum wells (QWs) [10–12], better heat sinking [13–17], higher injection efficiency [18–20], etc. Slow light has also been employed for SOA efficiency enhancement [21], but only optical pumping has been demonstrated. To the best of our knowledge, all these existing works focus on improving the SOA at the device level, so they are specific to a certain technology platform. They are all single-pass devices, so they still suffer from the problem of spatially inhomogeneous and inefficient carrier utilization.

Here, we propose a novel direction of SOA efficiency enhancement at the circuit level, leveraging on-chip mode-division multiplexing (MDM) [22–24]. In our approach, light gets reinjected back into the gain section, reusing the same gain material in both directions. Therefore, the interaction length is multiplied, and the available carriers are utilized in a more homogeneous way. Resonance is suppressed since each pass is spatially multiplexed in separate modes. Since it is a circuit-level method, it is generic and can be applied to many active–passive (A-P) platforms with distinct realizations of the components.

Efficiency enhancement using MDM has been demonstrated for linear devices such as thermo-optic [25] or electro-optic [26–28] modulators, but it has never been done for SOAs, which are highly nonlinear: the gain process is naturally exponential along the propagation direction, if not considering saturation. Therefore, compared to linear devices, a higher efficiency gain can be expected in SOAs with the same number of passes, or fewer passes may be needed to achieve a substantial efficiency boost. The challenge of integrating the MDM technique with active devices mainly

lies in their distinct waveguide cross sections. Low-loss, compact, and broadband MDM (de)multiplexers normally require high-confinement rectangular or ridge waveguides for efficient evanescent coupling [22,29]. Therefore, they are normally realized on high-confinement photonic platforms such as Si-on-insulator (SOI), which uses a thick dielectric layer for index contrast. In contrast, typical SOAs are realized in III-V material and have their optical modes buried in micrometer-scale semiconductor layer stacks for efficient electrical pumping [30].

In this paper, the integration challenge is tackled by the InP-membrane-on-silicon (IMOS) technology [31,32]. Via wafer-to-wafer bonding creating a high-index contrast cross section similar to that of SOI, the InP passive circuitry is miniaturized into a nanophotonic membrane. SOAs can be conveniently integrated into the same membrane by leveraging epitaxial growth at the wafer scale, allowing for a scalable PIC solution. Leveraging the active-passive IMOS technology, we demonstrate here, for the first time, significant SOA efficiency enhancement through an MDM double-pass (DP) gain section. The design, fabrication, and characterization results are subsequently presented in the following sections.

2. RESULTS

A. Circuit Design

The generic circuit architecture of the DP-SOA is shown in Fig. 1(a). The light path is as follows: input fiber grating coupler (FGC, TE_0); MDM (de)multiplexer (TE_0 passing through); SOA (TE_0 gain); MDM (de)multiplexer (TE_0 passing through); U-bend (TE_0); MDM (de)multiplexer (TE_0 converted to TE_1); SOA (TE_1 gain); MDM (de)multiplexer (TE_1 converted back to TE_0); output FGC (TE_0). Although a high-order mode is used inside the circuit, fiber interfacing is done using only the fundamental mode. As seen in Fig. 1(b), by breaking apart the U-bend and connecting to FGCs, an MDM 2 × 2 SOA is obtained, so the TE_0 and TE_1 gain channels can be independently accessed and characterized. This single-pass TE_0 channel can be used as a benchmark to quantify the gain performance of the DP-SOA.

All photonic components on the IMOS platform are based on a thin InP-based epilayer adhesively bonded on Si. The SOA gain section is based on a regrowth-free twin-guide scheme [31,32]. The active functional layers including n- and p-InP claddings, InGaAs metal contacting layer, and the core are epitaxially grown on top of the 300 nm thick i-InP layer, in which the passive waveguide and other photonic circuitries are fabricated. The core is made of InGaAsP with a bandgap corresponding to the 1250 nm

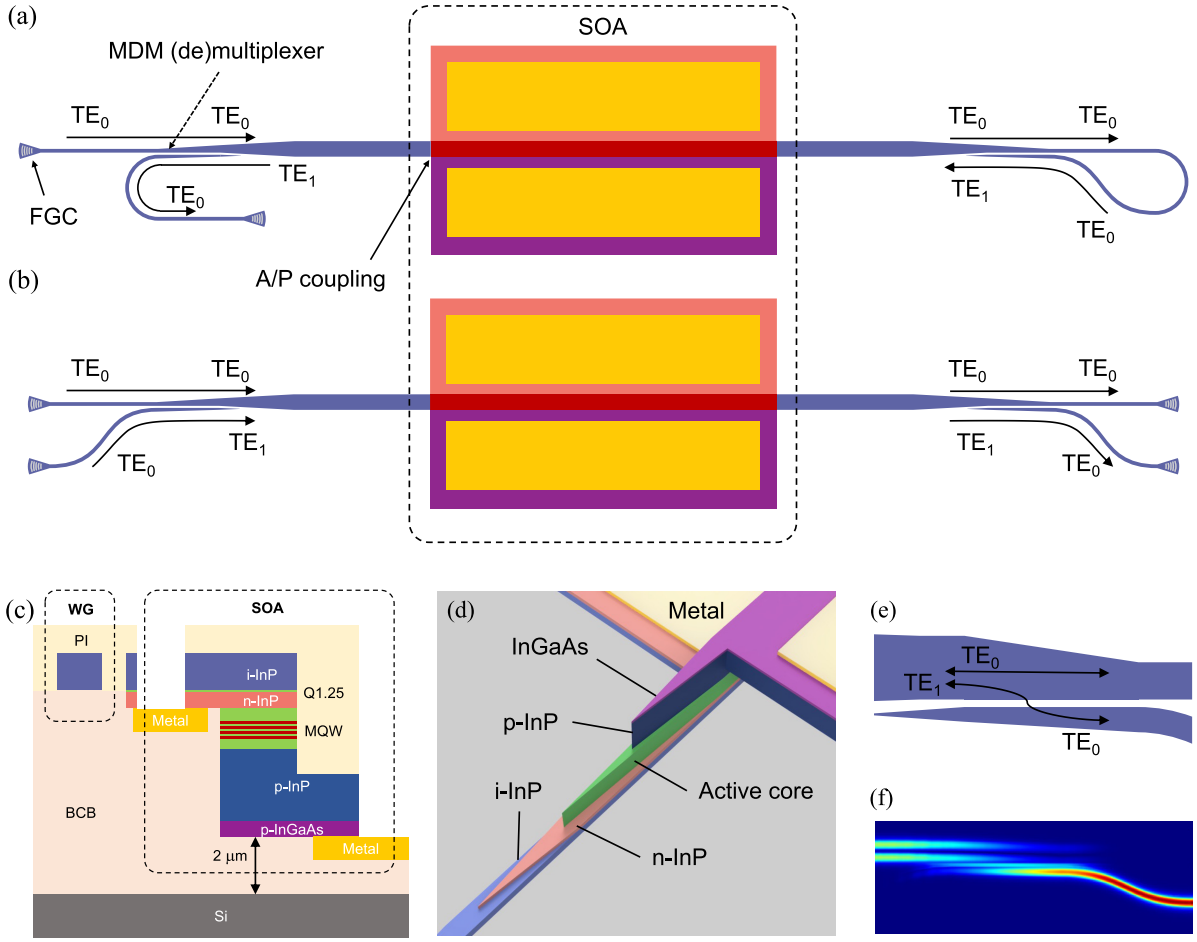

Fig. 1. Schematics of the MDM-SOA circuits (not to scale). (a) Top view of the DP-SOA. (b) Top view of the MDM 2 × 2 SOA. (c) Cross-sectional structure of the passive waveguide and SOA. The color scheme is the same as in (a). (d) 3D illustration of the SOA active–passive taper, looking from the substrate side. (e) Zoom-in schematics of the MDM (de)multiplexer. (f) Mode coupling between TE_0 and TE_1 through the MDM (de)multiplexer in (e).

wavelength (Q1.25) and contains a compressively strained 4-multi-QW (MQW). Halfway fabrication, the whole layer stack is flipped and buried into the benzo-cyclobutene (BCB) bonding layer, creating the cross section shown in Fig. 1(c). The whole wafer is also planarized and buried in polyimide (PI). The Q1.25 layer immediately under the i-InP layer is a wet etch-stop layer, which ensures an accurate etch depth for the SOA ridge and tapers without damaging the passive waveguide (see Section 1 in Supplement 1). The width of the SOA is designed to be 2.2 μm, supporting both TE_0 and TE_1 modes in the core region. Computed modal fields are shown in Supplement 1, Fig. S2. The confinement factors in the 4-MQW are calculated to be 4.31% and 4.29% for TE_0 and TE_1, respectively.

A-P coupling between the SOA and passive waveguide is done via a vertical evanescent taper, as seen in Fig. 1(d). In this taper, by separately tapering down the thick p-InP cladding to eliminate the vertical high-order cladding modes, unwanted mode conversions are suppressed (see Section 3 in Supplement 1 for details). The p-cladding, core, and n-cladding taper lengths are 10 μm, 35 μm, and 20 μm, respectively. The p-cladding and core taper both start at the gain section, and therefore the total taper length is 55 μm. The tip widths of the tapers are set to 200 nm for fabrication robustness [33]. According to eigenmode expansion (EME) simulations, a high 90% transmission is achieved for both TE_0 and TE_1 modes in this taper, if not considering material absorption.

Figure 1(e) shows the zoom-in schematics of the dual-core adiabatic tapers as an MDM (de)multiplexer. This MDM (de)multiplexer contains a multimode bus connecting directly to the SOA, and a TE_0 access waveguide for adiabatic coupling from/to the TE_1 mode in the bus waveguide. The gap between waveguides is designed to be 100 nm, allowing for simultaneous good manufacturability and a small footprint (50 μm coupling length). Detailed structural parameters and performance of the MDM (de)multiplexer can be found in Section 4 of Supplement 1. Figure 1(f) shows the light propagation through this MDM (de)multiplexer when TE_0 light of 1550 nm wavelength is launched in the access waveguide. This design is demonstrated to have high fabrication tolerance on waveguide width (±25 nm), low insertion loss (1 dB), and broad optical bandwidth (90 nm) [22].

B. Fabrication

The fabrication is done on both sides of the InP membrane (both before and after bonding to Si; see Section 1 in Supplement 1 for details) to realize the twin-guide S-shaped cross-sectional structure. After bonding, the distance between the InGaAs layer and Si layer is around 2 μm, as seen in Fig. 1(c). This BCB bonding layer planarizes surface topology, which enables high fabrication tolerance. The passive circuitries are fabricated after bonding from the back side of the original InP wafer and are therefore on top of the BCB layer. A microscope image of the fabricated DP-SOA is shown in Fig. 2(a). The zoom-in scanning electron microscope (SEM) images of the A-P taper before bonding and the coupling region of the MDM (de)multiplexer are shown as insets of the figure. Since e-beam lithography (EBL) is used for pattern definition, high overlay accuracy (∼20 nm) is achieved for all mask layers.

C. Enhanced Amplified Spontaneous Emission

The DP-SOA and a nearby 2 × 2 SOA with the same gain section dimensions (2.2 × 500 μm) are measured to characterize the gain enhancement. The wafer stage is kept at 10°C, and cleaved single-mode fibers (SMFs) are used for optical interfacing with the FGCs at an emission angle of 80° with respect to the waveguides. First, the LIV curves are obtained using a current source and broadband optical power meter for both channels of the 2 × 2 SOA and DP-SOA. As seen in Fig. 2(b), owing to the uniform wafer-scale process, the IV curves of the 2 × 2 SOA and DP-SOA overlap well with each other, and they both have a series resistance of ∼7 Ω. As can be seen, due to an extra pass in the gain section,

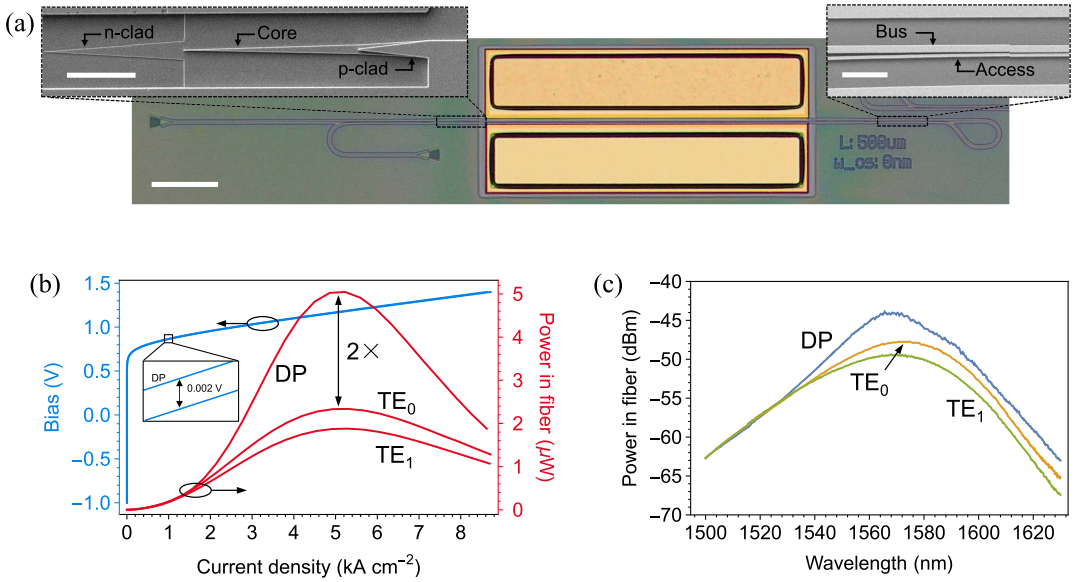

Fig. 2. ASE enhancement of the DP-SOA. (a) Microscope image of the fabricated DP-SOA (scale bar: 100 μm). The insets are zoom-in SEM images. Top left: SOA active–passive taper before bonding (scale bar: 10 μm). Here the i-InP waveguide is not yet fabricated. Top right: MDM (de)multiplexer fabricated after bonding. (b) LIV curves of the DP-SOA and reference 2 × 2 SOA of the same length. The received optical power for each SOA channel is labeled in the figure. Inset: Zoom-in of the IV curves around 1 kA cm^{-2}. The difference in bias at 1 kA cm^{-2} is 0.002 V. (c) ASE spectra of the DP-SOA and reference 2 × 2 SOA of the same length at a current density of 4.1 kA cm^{-2}.

2× higher ASE power is obtained at the same current density for the DP-SOA compared to the TE_0 channel of the 2 × 2 SOA (i.e., single pass). Since the TE_0 gain channel does not involve mode coupling over the MDM (de)multiplexer [22], the excess loss is negligible (Supplement 1, Fig. S6). Therefore, this channel can be used to benchmark the performance of the DP-SOA. The TE_1 ASE is lower than that of the TE_0, which is due to the TE_1 channel having: (1) extra loss from the MDM (de)multiplexer (Supplement 1, Fig. S6). 2) a slightly lower confinement factor and higher sidewall scattering loss in the gain section. Optical power saturation occurs at around 5 kA cm^{-2}, and it decreases beyond this point. ASE spectra collected by an optical spectrum analyzer (OSA) at the current density of 4.1 kA cm^{-2} for the DP-SOA and 2 × 2 SOA are shown in Fig. 2(c). Near-smooth spectra (<0.5 dB fluctuation) are obtained for both TE_0 and TE_1 channels, indicating the high mode conversion efficiency and low cross talk in the MDM (de)multiplexers. More significant fluctuations can be observed in the spectra of the DP-SOA. These fluctuations come from the residual optical feedback: ∼4% reflection of the SMF facet, ∼1% refection of the grating couplers, and ∼1% effective reflection from the MDM (de)multiplexers.

D. Enhanced Optical Gain and Power Efficiency

Since MDM SOA circuits involve more than one mode, measurement of optical gain is done by directly comparing the output and input optical powers. To measure the small-signal gain, an external tunable laser is used as the input, whose peak wavelength is tuned from 1520 nm to 1600 nm with a step of 2 nm. The on-chip input power after the FGC is set at −13.5 dBm. The input polarization is set for maximum optical transmission under a constant current injection. Since the FGCs and MQWs are designed for TE, and TM gain is far less than TE gain, a TE input polarization is assumed. Then, at various injection current densities, optical spectra are collected by an OSA for each input–output channel combination, for both the 2 × 2 SOA and DP-SOA. Then, the peak powers of the spectra are extracted. In this way, the broad ASE power can be excluded from the gain measurement. Nearby (<100 μm distance) reference waveguides are also measured at each corresponding wavelength point using the same configuration to calibrate out the FGC loss. The passive propagation loss in the access waveguides between FGCs and MDM (de)multiplexers is compensated for, and therefore zero-net-loss levels are obtained.

Figures 3(a)–3(c) show the received optical spectra at the current density of 4.1 kA cm^{-2}, with the blue dots indicating zero-net-loss levels, for the 2 × 2 SOA with input through the TE_0 port, input in the TE_1 port, and the DP-SOA, respectively. As can be seen, positive optical gain is achieved in the wavelength range of 1540–1600 nm for all three cases, and there are no signs of lasing of the SOAs themselves. As seen in Figs. 3(a) and 3(b), for the 2 × 2 SOA, the modal cross talk (TE_0-TE_1 and TE_1-TE_0 transmission) levels are −16.2 dB to 28.6 dB and −16.1 dB to −27.8 dB in the wavelength range of 1520–1570 nm for TE_0 and TE_1 input, respectively. This indicates that independently controllable and accessible gain channels are achieved. Generally, the cross talk increases as wavelength decreases, which could be due to stronger absorption and re-emission [34,35] in the gain section at shorter wavelengths.

Figure 3(d) shows the gain values by comparing the measured peak powers and zero-net-loss levels. As can be seen, the gain of the DP-SOA matches well with the summation of values obtained from the separate gain channels. At shorter wavelengths where the material gain is negative, the DP loss also corresponds well to the total loss in TE_0 and TE_1 channels. This indicates that light successfully travels through the gain section twice, and the zero-net-loss levels are correctly set. The 3 dB gain bandwidth measured for the DP-SOA is around 50 nm, confirming its broadband operation. The gain difference measured between TE_0 and TE_1 modes is

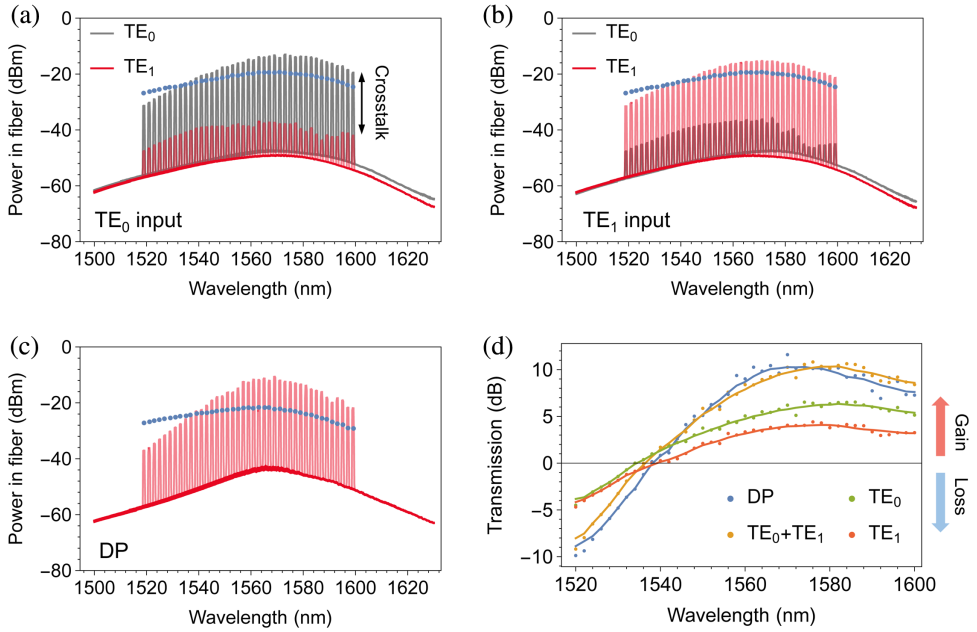

Fig. 3. Gain enhancement of the DP-SOA. (a), (b) Optical spectra of the 2 × 2 SOA obtained at current density of 4.1 kA cm^{-2}, using a tunable laser with −13.5 dBm on-chip input power. The spectra of different input wavelengths are overlapped, and the input and output channels are labeled on the bottom right and top right of the figures, respectively. Blue dots indicate zero-net-loss levels measured by reference waveguides. (c) Optical spectra of the DP-SOA at the same measurement conditions as in (a) and (b). (d) Optical transmission through the SOAs, obtained by subtracting the zero-net-loss levels from the peak powers in (a)–(c). Dots are actual data points, while solid curves are Wiener-filtered to eliminate the fluctuations from FGC and fiber reflections.

1.5–2.8 dB, which is partly due to the wavelength-dependent loss of the (de)multiplexers (Supplement 1, Fig. S6).

Compared to single-pass in TE_0, significant gain enhancement is achieved in the wavelength range of 1538–1600 nm for the DP-SOA. In the wavelength range of 1560–1580 nm, over 158% (58% more) optical gain is achieved, without increasing the operating current. The WPE ($WPE = P_{optical}/P_{electrical}$) can be calculated using the on-chip input and output optical powers ($P_{optical} = P_{out} - P_{in}$) and total electrical power ($P_{electrical} = VI$). In this 20 nm bandwidth, a > 180% extra WPE is achieved. At 1570 nm in particular, 11.6 dB gain is achieved for the DP-SOA, while the gain measured for single-pass TE_0 is 6.2 dB. Therefore, the net gain enhancement is 5.4 dB, or 87% more than the original value, for the same operating current. The WPE for single-pass and DP are 0.3% and 1.2% respectively. A 300% extra WPE is achieved. At shorter wavelengths of 1520–1536 nm, >100% absorption enhancement can be observed, which partly attributes to the extra loss from the MDM couplers.

Figures 4(a)–4(c) show the gain as a function of injection current density, at various wavelengths. As can be seen, the DP-SOA and single-pass TE_0 channel have similar zero-net-loss current densities, but beyond zero-net-loss, the DP gain increases faster and consistently outperforms the single-pass TE_0 gain. From another perspective, the same gain can be achieved with a lower injection current density, or less energy consumption, for the DP-SOA.

E. Saturation Effects

Saturation effects of the DP-SOA are measured by inserting sequentially an erbium-doped fiber amplifier (EDFA) and a variable optical attenuator (VOA) between the tunable laser and the input fiber. The measurement schematics can be seen in Supplement 1, Fig. S7. The optical power before the VOA is set to 17 dBm (tunable laser + EDFA), while the power at the input fiber is controlled by the VOA. Optical spectra are recorded at the output for each VOA setting, and the optical gain values are obtained by the peak powers subtracting zero-net-loss levels, the same as mentioned above. To calculate the on-chip input power, reference waveguides are measured to calibrate out the FGC loss as mentioned above.

Figure 5(a) shows the on-chip gain as a function of the on-chip input power for the DP-SOA at a current density of 4.1 kA cm^{-2} and 1570 nm wavelength. The same result for the TE_0 channel of the 2 × 2 SOA is also shown as a benchmark. As can be seen, compared to the benchmark, the DP-SOA consistently offers a higher gain of up to 5 dBm on-chip input power. At higher input power, saturation occurs. The input saturation power P_{sat} of the DP-SOA is −1.8 dBm, which is lower than that of the single-pass TE_0 (6.8 dBm). This is as expected since the DP-SOA has effectively a doubled interaction length, which significantly enhances light–matter interaction, and therefore, carriers are utilized more exhaustively and deplete faster. To further increase the saturation power, the optical confinement can be lowered, but at the cost of optical gain and WPE. In Fig. 5(a), optical gain increases slightly with input power before it goes down, which could be due to the beginning and end of the SOA being not well pumped and acting as saturable absorbers [36]. This can be solved by increasing the pad thickness and making the SOA taper passive.

Figure 5(b) shows the logarithmic plots of the WPE for both the DP-SOA and single-pass TE_0. As can be seen, since the extra gain is obtained without needing more current injection, up to 300% more WPE is obtained for the DP-SOA. The advantage shrinks as the gain becomes saturated, but the DP-SOA remains 100% more efficient until the on-chip input power reaches −5 dBm. At high input powers, the WPE goes down, and this is anticipated to result from increased nonlinear absorption.

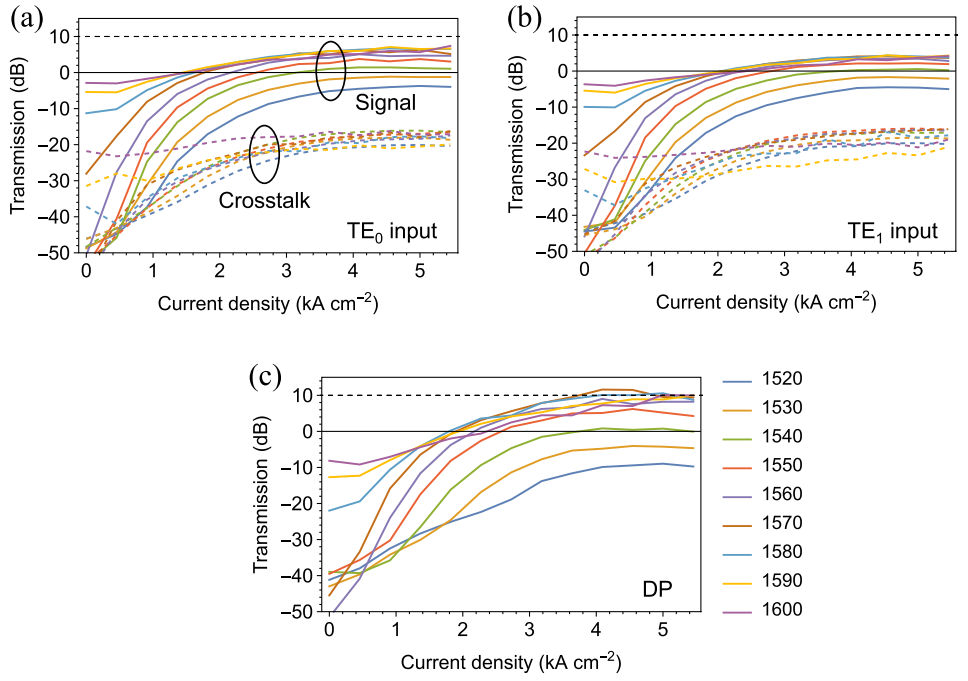

Fig. 4. (a), (b) Optical gain as functions of the injection current densities at various wavelengths, calculated by subtracting the zero-net-loss powers from the obtained peak powers. Solid lines and dashed lines are transmissions from the signal channels (TE_0-TE_0 and TE_1-TE_1) and cross talk channels (TE_0-TE_1 and TE_1-TE_0), respectively. (c) Optical transmission of the DP-SOA obtained using the same method as in (a) and (b).

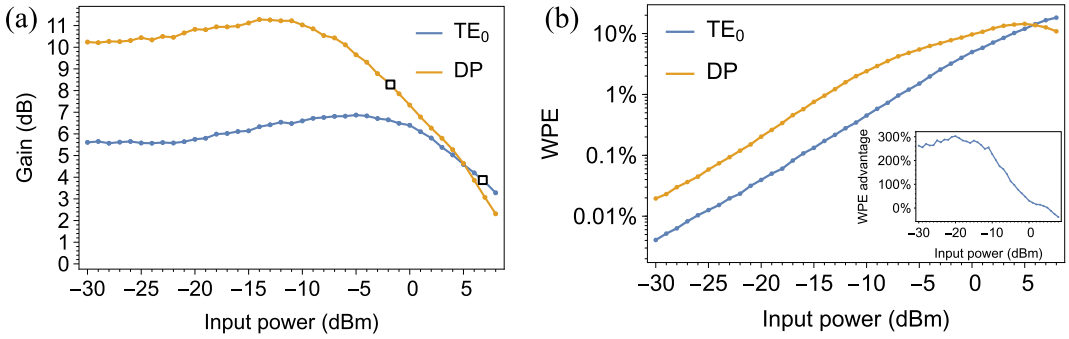

Fig. 5. Saturation effects of the DP-SOA. (a) On-chip gain as functions of on-chip input power at a wavelength of 1570 nm, measured with the TE_0 channel of the 2 × 2 SOA and DP-SOA. The input saturation points are indicated by empty squares in the figure. (b) WPE as functions of on-chip input power, calculated for the TE_0 channel of the 2 × 2 SOA and DP-SOA. The inset shows the extra amount of WPE obtained with the DP-SOA.

3. DISCUSSION

In this study, a maximum 6.2 dB single-pass gain is achieved at 4.1 kA cm^{-2}. This single-pass gain achieved is comparable to what has been realized on III-V-on-Si transfer-printing platforms with alignment-tolerant taper designs [37], if scaled proportionally in length. It is lower compared to those on native InP substrates with a similar geometric design and the same MQW, in which ∼10 dB optical gain can be achieved [38]. With specific optimizations on the material and geometric dimensions, gain values of more than 20 dB may be achieved [39]. However, as our work targets gain boost at the circuit level, its effectiveness is independent of the individual SOA component used. We expect a significant gain and efficiency boost if our method is combined with high-gain SOA with optimized component-level design.

The optical gain difference between the single-pass case in this work and a conventional SOA with a similar component-level design and the same MQW, but on the native substrate [38], is attributed to the following: the loss in the taper, thermal isolation due to the bonding layer, and the effectively deep-etched design. The passive loss in a single taper is simulated to be around 0.5 dB (Section 3 in Supplement 1), while the absorption is estimated to be 0.8 dB, assuming a 5000 dB cm^{-1} material loss in a single QW. Therefore, the coupling loss for one taper is estimated to be around 1.3 dB. This taper loss is comparable to heterogeneously integrated InP/Si SOAs, which have similar A-P tapers [40]. This supports our estimation as the refractive indices of Si and InP are close to each other, meaning similar taper dimensions. Based on this estimation, an 8.8 dB TE_0 single-pass gain in the active region can be achieved without this coupling loss. The remaining ∼1 dB difference is attributed to worse thermal dissipation and higher sidewall recombination due to the more exposed active section. It should be noted that neither of these is a fundamental limitation: the taper can be made passive through QW intermixing [41] or ion implantation, or even be completely eliminated using butt-joint regrowth [42,43]; the thermal performance can be improved by thermal shunting to the silicon substrate [14], or using high-thermal-conductivity substrates [16]. The sidewall recombination velocity can be greatly reduced by wet chemical treatments [18].

Excluding grating couplers, which is not a fundamental limiting factor, the maximum possible gain of the DP-SOA is determined by the cross talk of the MDM (de)multiplexer, since cross talk manifests itself as reflections into the same mode at the U-bend. In this work, −20.3 dB cross talk is obtained, but this may be further reduced to −33 dB by altering the waveguide design [44]. This level of reflection is comparable to that in bulk InP SOAs with butt-joint A-P interfaces [45].

In conclusion, we demonstrate that gain and efficiency can be significantly enhanced by reinjecting the amplified light for a second pass through the SOA gain section. Each pass in the SOA is in separate transversal modes, so resonance is suppressed and broadband operation is achieved. Light also passes through the gain section from opposite directions, therefore homogeneously utilizing the available carriers. Compared to the single-pass case, the ASE power is improved by >100%, and 58%–87% more small-signal gain is obtained at the same injection current in the wavelength range of 1560–1580 nm; 300%–100% more WPE is achieved for on-chip input powers up to −5 dBm.

Since the method demonstrated in this paper works at the circuit level, it can be exploited in combination with other efficiency enhancement methods to achieve even better performance. It also allows gain and efficiency enhancement without changing the SOA layer stack itself, providing more compatibility and versatility in circuit design. Although demonstrated on the InP membrane platform, in principle, the concept is applicable to a wide range of A-P integration platforms including hybrid, heterogeneous, or butt-joint technologies, such as III-V/Si platforms with Si or SiN_x waveguides. With the increasing demand for building block performance in densely integrated PICs, this work may be used in various applications such as optical beam steering, neuromorphic photonics, photonic matrix computation, photonic switching, etc. The DP-SOA may also be used to realize novel laser types, and the design principle can be leveraged to boost the extinction ratio of electro-absorption modulators without increasing the length, so modulation speed will not be compromised. It is also worth noting that this is the first time that MDM is realized in active photonic circuits on-chip, which opens up new opportunities in device and circuit design, such as multi-wavelength lasers or channel multi-casting.

Funding. National Science Fund for Distinguished Young Scholars (61725503); Nederlandse Organisatie voor Wetenschappelijk Onderzoek (Research Centre for Integrated Nanophotonics).

Acknowledgment. The NanoLab@TU/e cleanroom facility is acknowledged for the fabrication.

Disclosures. The authors declare no conflicts of interest.

Data availability. Data underlying the results are available upon reasonable request.

Supplemental document. See Supplement 1 for supporting content.

REFERENCES

1. M. J. R. Heck and J. E. Bowers, "Energy efficient and energy proportional optical interconnects for multi-core processors: driving the need for on-chip sources," IEEE J. Sel. Top. Quantum Electron. **20**, 332–343 (2014).
2. D. A. B. Miller, "Attojoule optoelectronics for low-energy information processing and communications," J. Lightwave Technol. **35**, 346–396 (2017).
3. F. Kish, V. Lal, P. Evans, *et al.*, "System-on-chip photonic integrated circuits," IEEE J. Sel. Top. Quantum Electron. **24**, 6100120 (2018).
4. Q. Cheng, S. Rumley, M. Bahadori, and K. Bergman, "Photonic switching in high performance datacenters [invited]," Opt. Express **26**, 16022–16043 (2018).
5. C.-P. Hsu, B. Li, B. Solano-Rivas, A. R. Gohil, P. H. Chan, A. D. Moore, and V. Donzella, "A review and perspective on optical phased array for automotive LiDAR," IEEE J. Sel. Top. Quantum Electron. **27**, 8300416 (2021).
6. L. A. Coldren, S. W. Corzine, and M. Mashanovitch, *Diode Lasers and Photonic Integrated Circuits*, 2nd ed., Wiley series in microwave and optical engineering No. 218 (Wiley, 2012).
7. T. Hiratani, D. Inoue, T. Tomiyasu, K. Fukuda, T. Amemiya, N. Nishiyama, and S. Arai, "High-efficiency operation of membrane distributed-reflector lasers on silicon substrate," IEEE J. Sel. Top. Quantum Electron. **23**, 3700108 (2017).
8. S. Matsuo, T. Fujii, K. Hasebe, K. Takeda, T. Sato, and T. Kakitsuka, "Directly modulated buried heterostructure DFB laser on SiO_2/Si substrate fabricated by regrowth of InP using bonded active layer," Opt. Express **22**, 12139–12147 (2014).
9. T. Fujii, K. Takeda, H. Nishi, N.-P. Diamantopoulos, T. Sato, T. Kakitsuka, T. Tsuchizawa, and S. Matsuo, "Multiwavelength membrane laser array using selective area growth on directly bonded InP on SiO_2/Si," Optica **7**, 838–846 (2020).
10. C.-E. Zah, R. Bhat, B. N. Pathak, F. Favire, W. Lin, M. C. Wang, N. C. Andreadakis, D. M. Hwang, M. A. Koza, T.-P. Lee, Z. Wang, D. Darby, D. Flanders, and J. J. Heieh, "High-performance uncooled 1.3-μm $Al_xGa_yIn_{(1-x-y)}As$/InP strained-layer quantum-well lasers for subscriber loop applications," IEEE J. Quantum Electron. **30**, 511–523 (1994).
11. S. Cheung, K. Shang, Y. Kawakita, and S. J. Ben Yoo, "Efficient III-V/Si hybrid SOAs for optical interconnects," in *CLEO* (OSA, 2015), paper STu4F.4.
12. S. Cheung, Y. Kawakita, K. Shang, and S. J. B. Yoo, "Theory and design optimization of energy-efficient hydrophobic wafer-bonded III–V/Si hybrid semiconductor optical amplifiers," J. Lightwave Technol. **31**, 4057–4066 (2013).
13. F. Lemaître, V. Rustichelli, H. P. M. M. Ambrosius, R. Brenot, and K. A. Williams, "Thermal comparison of buried-heterostructure and shallow-ridge lasers," Proc. SPIE **10526**, 229–234 (2018).
14. C. Zhang, D. Liang, G. Kurczveil, J. E. Bowers, and R. G. Beausoleil, "Thermal management of hybrid silicon ring lasers for high temperature operation," IEEE J. Sel. Top. Quantum Electron. **21**, 385–391 (2015).
15. G. Gilardi, W. Yao, H. R. Haghighi, M. K. Smit, and M. J. Wale, "Substrate thickness effects on thermal crosstalk in InP-based photonic integrated circuits," J. Lightwave Technol. **32**, 3061–3066 (2014).
16. S. Yamaoka, N.-P. Diamantopoulos, H. Nishi, R. Nakao, T. Fujii, K. Takeda, T. Hiraki, T. Tsurugaya, S. Kanazawa, H. Tanobe, T. Kakitsuka, T. Tsuchizawa, F. Koyama, and S. Matsuo, "Directly modulated membrane lasers with 108 GHz bandwidth on a high-thermal-conductivity silicon carbide substrate," Nat. Photonics **15**, 28–35 (2021).
17. M. Takenaka and S. Takagi, "InP-based photonic integrated circuit platform on SiC wafer," Opt. Express **25**, 29993–30000 (2017).
18. A. Higuera-Rodriguez, B. Romeira, S. Birindelli, L. E. Black, E. Smalbrugge, P. J. van Veldhoven, W. M. M. Kessels, M. K. Smit, and A. Fiore, "Ultralow surface recombination velocity in passivated InGaAs/InP nanopillars," Nano Lett. **17**, 2627–2633 (2017).
19. G. Crosnier, A. Bazin, V. Ardizzone, P. Monnier, R. Raj, and F. Raineri, "Subduing surface recombination for continuous-wave operation of photonic crystal nanolasers integrated on silicon waveguides," Opt. Express **23**, 27953–27959 (2015).
20. V. Rustichelli, C. Calo, H. Ambrosius, and K. Williams, "Fully integration of buried-hetrostrucutres in the TU/e generic platform," IEEE J. Sel. Top. Quantum Electron. **8** (2017).
21. S. Ek, P. Lunnemann, Y. Chen, E. Semenova, K. Yvind, and J. Mork, "Slow-light-enhanced gain in active photonic crystal waveguides," Nat. Commun. **5**, 5039 (2014).
22. Y. Wang, Y. Wei, V. Dolores-Calzadilla, K. Williams, M. Smit, D. Dai, and Y. Jiao, "Mode division multiplexing on an InP membrane on silicon," Opt. Lett. **47**, 4004–4007 (2022).
23. L.-W. Luo, N. Ophir, C. P. Chen, L. H. Gabrielli, C. B. Poitras, K. Bergmen, and M. Lipson, "WDM-compatible mode-division multiplexing on a silicon chip," Nat. Commun. **5**, 3069 (2014).
24. D. Dai, J. Wang, and Y. Shi, "Silicon mode (de)multiplexer enabling high capacity photonic networks-on-chip with a single-wavelength-carrier light," Opt. Lett. **38**, 1422–1424 (2013).
25. S. A. Miller, Y.-C. Chang, C. T. Phare, M. C. Shin, M. Zadka, S. P. Roberts, B. Stern, X. Ji, A. Mohanty, O. A. J. Gordillo, U. D. Dave, and M. Lipson, "Large-scale optical phased array using a low-power multi-pass silicon photonic platform," Optica **7**, 3–6 (2020).
26. K. Zhang, W. Sun, Y. Chen, H. Feng, Y. Zhang, Z. Chen, and C. Wang, "A power-efficient integrated lithium niobate electro-optic comb generator," Commun. Phys. **6**, 17 (2023).
27. H. Huang, X. Han, A. Balčytis, A. Dubey, A. Boes, T. G. Nguyen, G. Ren, M. Tan, Y. Tian, and A. Mitchell, "Non-resonant recirculating light phase modulator," APL Photon. **7**, 106102 (2022).
28. Y. Yin, J. Li, Y. Xu, H. K. Tsang, and D. Dai, "Silicon-graphene photonic devices," J. Semicond. **39**, 061009 (2018).
29. D. Dai, C. Li, S. Wang, H. Wu, Y. Shi, Z. Wu, S. Gao, T. Dai, H. Yu, and H.-K. Tsang, "10-channel mode (de)multiplexer with dual polarizations," Laser Photon. Rev. **12**, 1700109 (2018).
30. M. Smit, X. Leijtens, H. Ambrosius, *et al.*, "An introduction to InP-based generic integration technology," Semicond. Sci. Technol. **29**, 083001 (2014).
31. Y. Jiao, J. van der Tol, V. Pogoretskii, *et al.*, "Indium phosphide membrane nanophotonic integrated circuits on silicon," Phys. Status Solidi A **217**, 1900606 (2020).
32. Y. Jiao, N. Nishiyama, J. van der Tol, J. van Engelen, V. Pogoretskiy, S. Reniers, A. A. Kashi, Y. Wang, V. D. Calzadilla, M. Spiegelberg, Z. Cao, K. Williams, T. Amemiya, and S. Arai, "InP membrane integrated photonics research," Semicond. Sci. Technol. **36**, 013001 (2020).
33. V. Pogoretskiy, *Nanophotonic Membrane Platform for Integrated Active Devices and Circuits* (Technische Universiteit Eindhoven, 2019).
34. Y. Feng, B. M. Zhang, J. Zhao, S. Zhu, J. H. V. Price, and J. Nilsson, "Absorption measurement errors in single-mode fibers resulting from re-emission of radiation," IEEE J. Quantum Electron. **53**, 6800611 (2017).
35. Y. Fang, H. Wei, Q. Dong, and J. Huang, "Quantification of re-absorption and re-emission processes to determine photon recycling efficiency in perovskite single crystals," Nat. Commun. **8**, 14417 (2017).
36. T. Nakahara and R. Takahashi, "Self-stabilizing optical clock pulse-train generator using SOA and saturable absorber for asynchronous optical packet processing," Opt. Express **21**, 10712–10719 (2013).
37. B. Haq, S. Kumari, K. Van Gasse, J. Zhang, A. Gocalinska, E. Pelucchi, B. Corbett, and G. Roelkens, "Micro-transfer-printed III-V-on-silicon C-band semiconductor optical amplifiers," Laser Photon. Rev. **14**, 1900364 (2020).
38. D. Pustakhod, K. Williams, and X. Leijtens, "Fast and robust method for measuring semiconductor optical amplifier gain," IEEE J. Sel. Top. Quantum Electron. **24**, 3100309 (2018).
39. C. Caillaud, G. Glastre, F. Lelarge, R. Brenot, S. Bellini, J.-F. Paret, O. Drisse, D. Carpentier, and M. Achouche, "Monolithic integration of a semiconductor optical amplifier and a high-speed photodiode with low polarization dependence loss," IEEE Photon. Technol. Lett. **24**, 897–899 (2012).
40. P. Kaspar, G. de Valicourt, R. Brenot, M. A. Mestre, P. Jenneve, A. Accard, D. Make, F. Lelarge, G.-H. Duan, N. Pavarelli, M. Rensing, C. Eason, P. O'Brien, S. Olivier, S. Malhouitre, C. Kopp, C. Jany, and S. Menezo, "Hybrid III-V/silicon SOA in optical network based on advanced modulation formats," IEEE Photon. Technol. Lett. **27**, 2383–2386 (2015).
41. N. Sekine, K. Toprasertpong, S. Takagi, and M. Takenaka, "Active-passive integration on III-V-OI platform using quantum well intermixing," in *Conference on Lasers and Electro-Optics* (2020), pp. 2.
42. S. Matsuo, A. Shinya, T. Kakitsuka, K. Nozaki, T. Segawa, T. Sato, Y. Kawaguchi, and M. Notomi, "High-speed ultracompact buried heterostructure photonic-crystal laser with 13 fJ of energy consumed per bit transmitted," Nat. Photonics **4**, 648–654 (2010).

43. Y. Wang, J. van Engelen, R. van Veldhoven, T. de Vries, V. Dolores-Cazadilla, M. Smit, K. Williams, and Y. Jiao, "Versatile butt-joint regrowth for dense photonic integration," Opt. Mater. Express **11**, 2478–2487 (2021).
44. C. Li and D. Dai, "Low-loss and low-crosstalk multi-channel mode (de)multiplexer with ultrathin silicon waveguides," Opt. Lett. **42**, 2370–2373 (2017).
45. Y. Barbarin, E. Bente, C. Marquet, and E. Leclere, "Butt-joint reflectivity and loss in InGaAsP/InP waveguides," in *12th European Conference on Integrated Optics* (2005).